PURPOSE-LED
PUBLISHING™

PAPER • OPEN ACCESS

On the origins of the continuum radiation of an underwater nanosecond pulsed discharge: an absolute-intensity optical emission spectroscopy study

On the origins of the continuum radiation of an underwater nanosecond pulsed discharge: an absolute-intensity optical emission spectroscopy study

Marien Simeni Simeni⬤, Yuchen Luo and Peter J Bruggeman*⬤

Department of Mechanical Engineering, University of Minnesota, 111 Church Street SE, Minneapolis, MN 55455, United States of America

E-mail: pbruggem@umn.edu

CrossMark

Abstract

The plasma properties of an underwater nanosecond pulsed discharge remain not fully understood despite being extensively studied for several decades. In this work, we focus on the continuum radiation generated in such discharges. The discharge is characterized by power measurements as well as by absolute emission spectroscopy. When observed, Stark broadenings of H_α, H_β and O (777 nm) are employed for electron number densities measurements. The discharge was generated by a 10 ns main voltage pulse followed by multiple secondary pulses, which last up to 4 μs after the primary pulse. It is shown that a peak power of 3.5 MW and energy of 35 mJ is coupled during the main voltage pulse. A quantitative estimation of the different possible continuum radiation sources is performed through analytical calculations. This includes emission (blackbody, free–bound and free–free bremsstrahlung radiations) and absorption (electron–ion and electron–neutral free–free inverse bremsstrahlung) mechanisms. Our results suggest that electron–neutral free–free bremsstrahlung is the principal mechanism responsible for the strong continuum radiation observed experimentally during the primary pulse. We also show that self-absorption through electron–neutral (and electron–ion) inverse bremsstrahlung plays an important role in the main discharge pulse. Further, our results indicate the non-negligible additional contribution of the H_2 continuum during the first reflected pulse which is likely ignited in bubbles generated by the first discharge pulse.

Keywords: underwater plasma, nanosecond pulsed discharge, continuum radiation, absolute-intensity OES

---

* Author to whom any correspondence should be addressed.

1. Introduction

The study of plasmas generated in and in contact with liquids is motivated by the multiple and ever-growing application areas. Water treatment (Foster 2017), upgrading of heavy oils (Hueso *et al* 2009), hydrocarbon reforming (Levko *et al* 2017), spectrochemical analysis of elemental composition of solutions (Fichet *et al* 2001, Webb and Hieftje 2009), H_2 and H_2O_2 production (Mededovic and Locke 2007), decontamination (Sato *et al* 1996), and extreme ultraviolet (EUV) lithography at 13.5 nm (Versolato 2019) using liquid tin droplets are just a few highlights of the significant potential of these plasmas.

Specifically for underwater electrical discharges, our understanding of the discharges initiation mechanisms, dynamics and even chemical processes remains limited despite decades of research (Bruggeman *et al* 2009, Bruggeman *et al* 2016). Nonetheless, discharges in liquid water can host very extreme environments characterized by high pressures, temperatures and electron densities (Locke *et al* 2006, Bruggeman *et al* 2016), even capable of reaching supercritical states of matter (Grosse *et al* 2019) similar to laser-produced plasmas (Versolato 2019). The plasma parameters of discharges in liquids are strongly dependent on the excitation voltages waveforms, electrical conductivity of the liquid and electrodes geometries (Ceccato *et al* 2010) with pressures reaching values up to tens of GPa (Marinov *et al* 2014). This has been confirmed directly through interferometric measurements (An *et al* 2007, Hoffer *et al* 2020, Simek *et al* 2020a, Hoffer *et al* 2021). As a result of the high-pressure regime, underwater discharges exhibit a highly transient nature.

In the literature, a clear distinction is made between discharges in liquid water generated using excitation voltage waveforms with either milliseconds/microseconds or nanoseconds characteristic times. It is generally accepted that long duration voltage pulses (with a slow rise time) are generated in gas microbubbles, through the evaporation of the surrounding liquid water following Joule heating (Bruggeman *et al* 2009, Wen *et al* 2020). Conversely, for nanosecond rise times at sufficiently high voltage and low repetition rate, studies suggested the possibility of the plasma being generated directly in the liquid phase (Starikovskyi *et al* 2011, Dobrynin *et al* 2013). The nanosecond breakdown characteristic time excludes the possibility of a breakdown driven by microbubble dynamics, which has a microsecond characteristic time (characteristic inertial time). To explain these experimental observations, Shneider and Pekker argued that a high and fast rising electric field localized at the sharp tip of an immersed electrode could generate cracks (nanopores) in the liquid, breaking its continuity through the process of electrostriction (Shneider and Pekker 2013, Pekker and Shneider 2015). With the subsequent breakdown occurring because of the substantial energy gained by the electrons in the electrostriction-induced cavitation areas. More recently, Li *et al* (2020) performed a comprehensive numerical study of the ignition process. They modeled the cavitation, nanopores expansion and electron multiplication

phases. Their results suggest that direct ignition of underwater nanosecond discharges in liquid water can occur as a result of the electrostrictive forces (Li *et al* 2020). Regarding the electron multiplication process, numerical investigations were conducted by Bonaventura *et al* (2021), where scaling laws for electron propagation were introduced (Bonaventura *et al* 2021). However, it is equally important to note that electrostriction is not the only initiation mechanism discussed in the literature. Other candidate mechanisms include for example the Auger (Lewis 2003), Lippmann (Lewis 2003) and proton hopping (Vegiri 2004) effects among many others (Kolb *et al* 2008).

As demonstrated by Simek *et al* (2017) and pointed out by Grosse *et al* (2019) the transient nature of nanosecond underwater discharges commands highly time-resolved measurements. Currently, most of the experimental investigations have employed imaging and UV to near-IR optical emission spectroscopy techniques. Recent studies have been focused on positive polarity voltage pulses excitation schemes. One of the notable results of the time-resolved studies is the observation of distinct dark and luminous phases during the ignition (Simek *et al* 2020b). Focusing on luminous phases, previous observations reported: (1) a first luminous phase characterized by an intense light emission localized near the high-voltage (HV) electrode coinciding in time with a broadband (UV to near-IR) continuum emission with no atomic lines observed. (2) A second luminous phase occurring a few tens/hundreds of nanoseconds (depending on the setup) later, which features propagating streamers, coinciding with strong emission of atomic lines notably hydrogen Balmer series lines (H_α, H_β, H_γ), O (triplet at 777 nm and singlet 840 nm) and then molecular band emissions (OH) (Simek *et al* 2017, Pongrac *et al* 2018, Grosse *et al* 2019, Von Keudell *et al* 2020).

The second luminous phase has been in the spot light because of its attractiveness to derive plasma parameters (n_e, T_e VS. time) using Stark broadening of the aforementioned atomic lines. However, to this aim, the quantification of other broadening mechanisms such as Doppler and Van der Waals broadening is required. Van der Waals broadening especially causes a problem because of the high pressure observed during the ignition phase. If pressure relaxation following the bubble expansion at ignition has not fully occurred, then during the second phase when atomic lines are observed, one cannot neglect Van der Waal broadening from the measured widths of the spectra. Therefore, a disentanglement (deconvolution) method becomes crucial. In a series of papers (Grosse *et al* 2019, 2020, Von Keudell *et al* 2020) researchers from Bochum University addressed this issue. They used a cavitation model based on the Rayleigh–Plesset equations to match the bubble hydrodynamics (expansion and collapse) experimentally observed through shadow-graph images. From the model, they were able to extract the time-dependent gas temperature and pressure during the ignition and expansion phases of the discharge. Thanks to these values, the disentanglement between Van der Waals and Stark broadening was made possible. They found

electron densities up to 10^{25} m^{-3} for a peak applied voltage of 26 kV and a liquid conductivity of 2 μS cm^{-1}. Nonetheless, the analysis remains indirect and is based on the interpretation of the bubble dynamics post discharge.

The first luminous phase of the discharge initiation has been less used to infer plasma parameters because of the uncertainties regarding the origins of the broadband continuum emission. Simek *et al* (2017) listed many possibilities: bremsstrahlung radiation, blackbody radiation, H$_2$ continuum (a$^3\Sigma_g^+ \rightarrow$ b$^3\Sigma_u^+$), and H$_2$O continuum ($\tilde{C}^1$B$_1 \rightarrow \tilde{A}^1B_1$). These possibilities were narrowed down to the first two because H$_2$ and H$_2$O continua are only observed in limited spectral ranges, inconsistent with the broad UV to near-infrared experimental observations. To distinguish between bremsstrahlung and blackbody radiation, the authors corrected the measured experimental spectra to account for the spectral response of the detection systems. Note that no absolute calibrations were reported. Following the spectral correction, characteristic increasing emission intensities from the near-infrared to the UV spectral range were obtained by both (Šimek *et al* (2017) and Grosse *et al* (2020). However, because of the similarities between the theoretical shapes of the blackbody and bremsstrahlung radiation, Simek *et al* concluded that the observed emission was due to bremsstrahlung radiation with the shape of the spectra depending on the electron energy distribution function (EEDF) which was seemingly arbitrary assumed to be a Gaussian function (Bilek *et al* 2021). Grosse *et al*, however opted for blackbody radiation. Grosse *et al* argued in favor of blackbody radiation coming from the hot surface of the HV tungsten electrode because of a better fit of the spectrum to the experimental data (Grosse *et al* 2020). However, they stated that the spectral signature was in fact that of a grey body instead of a blackbody, hence implying a non-ideal emissivity, consistent with the inhomogeneous surface of the tungsten pin apparent from scanning electron microscope observations. Interestingly, this would only be consistent with the corrected emission spectra (wavelength sensitivity accounted for) in case of a wavelength-independent relative emissivity of the tungsten electrode, which seems unlikely. Further, when performing calculations of the shape of the continuum spectrum arising from bremsstrahlung radiation, only electron–neutral free–free bremsstrahlung was considered, and a constant electron–neutral momentum transfer cross-section was employed. Furthermore, potential opacity effects due to self-absorption were not considered. Such effects are expected to be of importance in the case of the first phase because of the very high densities (high pressure), up to about 10^{28} m^{-3} (Marinov *et al* 2014, Hoffer *et al* 2020, Li *et al* 2020). Noteworthy, tungsten electrodes tip radii of curvature for the latter experiments were systematically smaller (hence electric fields significantly higher) than those from Simek *et al*. This might have led to striking differences in continuum radiation. While erosion of the electrode tips was typically observed by the research group from Bochum, electrodes from the research group from Prague appear to last very long. Erosion of electrode tips leads for example to particle formation (Krettek *et al* 2024), which could be a source of blackbody radiation.

We hypothesize that these apparent conflicting interpretations for very similar plasma conditions can be resolved by measuring absolute intensities. This led us to revisit the excellent work from the research groups in Prague and Bochum but with an emphasis on absolute optical emission spectroscopy (OES) measurements enabling us to clearly assess in more detail and extend the analysis of the origins of the observed broadband continuum radiation. We also investigate the contribution of bremsstrahlung emission to the continuum emission in detail, considering both electron–neutral and electron–ion (free–free and free–bound) radiation using electron energy-dependent momentum transfer cross sections from the literature while accounting for self-absorption effects.

2. Experimental setup and methods

2.1. Reactor assembly

Figure 1(a) shows a schematic of the discharge reactor setup. The discharge is generated at the tip of a sharpened tungsten needle (radius of curvature ∼100 μm) in a single electrode geometry. The HV electrode is located at the center of the 9 cm wide cubic metal vessel filled with liquid. The electrically grounded stainless steel vessel can be filled with up to 300 ml of solution. For our experiments, we used NaCl (Sigma-Aldrich, 99% purity) and distilled water to prepare saline water solutions with an electrical conductivity of 250 μS cm^{-1}. The immersed tungsten electrode is powered by a HV nanosecond power supply (FID Technology GmbH, FPG 50–1NM12). The HV pulser can deliver positive voltage pulses up to 50 kV amplitude with 3–5 ns rise time, 10–15 ns pulse width (FWHM), and up to 1 kHz repetition frequency. Besides, the pulser and high voltage electrode are connected through a 20 m long, 50 Ω coaxial cable transmission line (RG217) along with an impedance-matched home-made insulated rod-vessel assembly. Additionally, the test cell is equipped with three quartz windows (5 cm diameter) enabling optical access to the discharge area (see further). Finally, a four channels delay generator (BNC 577) is used to externally trigger the HV power supply and serves as the master clock for the timing of the experiment with a temporal resolution of 2 ns mainly due to the jitter in the discharge generation. The discharge assembly, as pictured in figure 1(b) is mounted on a three-axis translation stage to facilitate the alignment of the discharge with the optical system. A more detailed view of the reactor and its components is given by the 3D CAD model depicted in figure 1(c).

2.2. Electrical measurements using back-current shunt (BCS), D-dot and B-dot probes

Figure 1(a) also displays the electrical probes employed for measurements of the power coupled in the discharge. Accurate electrical measurements for such a system are challenging because most of the commercial probes cannot meet the high
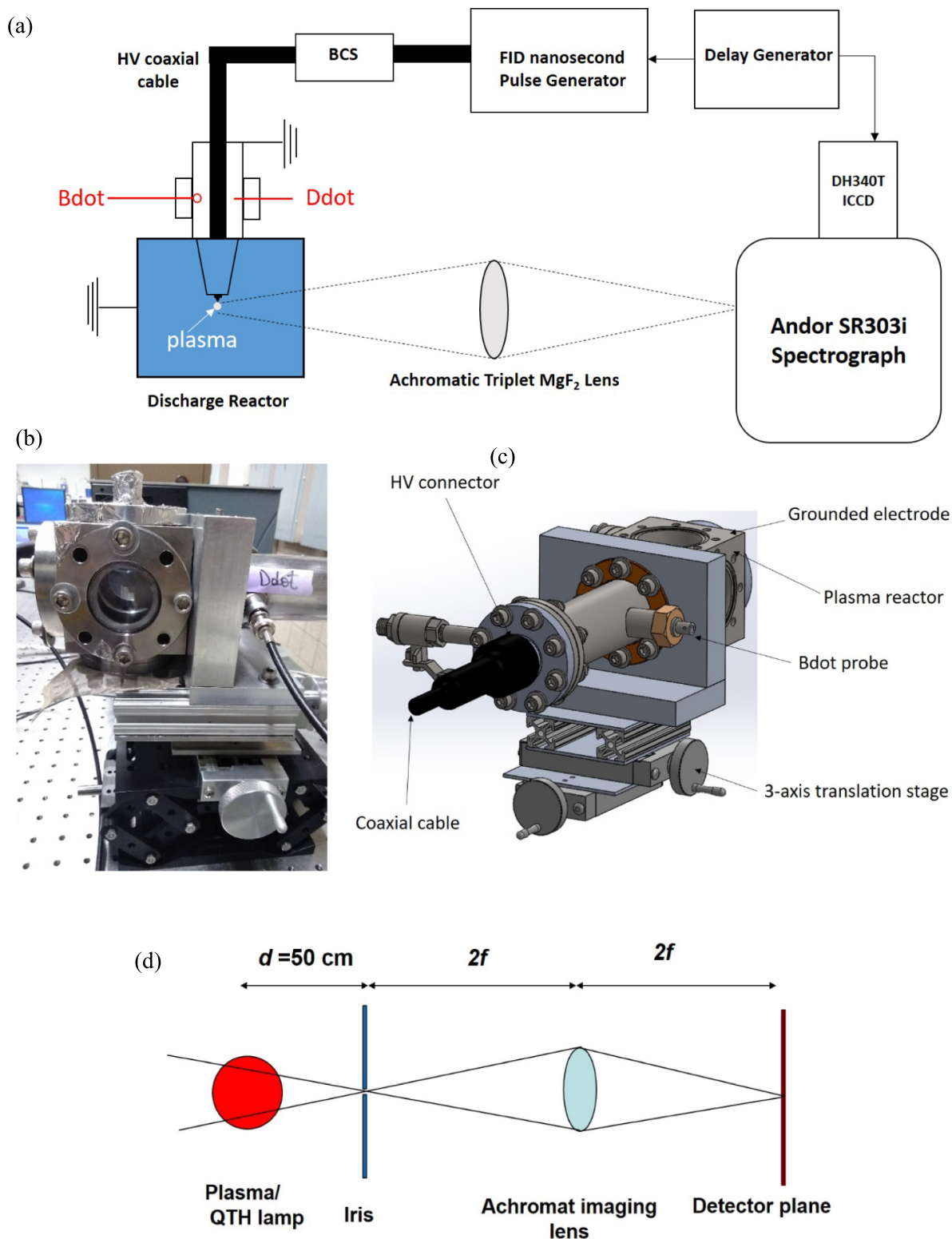
Figure 1. (a) Schematic diagram of the experimental setup used for OES and electrical measurements. (b) Photograph of the discharge reactor. (c) Detailed 3D view of the discharge reactor assembly. (d) Schematic of the setup used for absolute OES measurements (not to scale).

bandwidth along with high voltages and high currents requirements typical of such discharges. Two approaches (based on three different sensors) were used to resolve the fast-rising electrical signals and mitigate electromagnetic interference

(EMI) issues while performing the measurements. A BCS on one hand and a home-made capacitive voltage divider (D-dot) and inductively coupled current sensor (B-dot) on the other hand. The electrical waveforms measured by these probes

were recorded using a four-channel digital oscilloscope with a 1 GHz bandwidth (LeCroy WaveSurfer10, 10 GSa s^{-1}). The low-inductance BCS was inserted at the middle position, in the shielding layer of the coaxial transmission line and calibrated using a DC power supply with a known resistor in series. The BCS is a mature technique and details pertaining to the separation of the forward and reflected pulse trains can be found in (Babicky *et al* 2017). After separation of the forward and reflected waves, the calibrated BCS signals yield (forward) voltage and current waveforms in the central rod of the transmission line. However, for our experimental conditions, because of the long-lasting pulse reflections (see results section), the 20 m long transmission line does not ensure a full separation of the forward and reflected wave trains. Therefore, two home-made probes were employed along with the BCS. D-dot and B-dot probes were mounted closer (∼10 cm distance) to the needle electrode, on the rod-vessel assembly. The D-dot and B-dot probes are used to measure the discharge voltage and current signals, respectively. Details about their working principles can be found in (Huiskamp *et al* 2016). These probes were calibrated using the calibrated BCS, assuming that the plasma generated in the single electrode (anode) configuration is equivalent to an open load. Results obtained using the two different approaches are within 15%, with a main contribution arising from the uncertainty of the calibration coefficients (Luo 2019). For that reason, for the remainder of the manuscript, we only report the electrical characterization obtained from the D-dot and B-dot probes measurements.

2.3. Imaging and OES measurements

In addition to the electrical diagnostics, direct imaging and OES measurements were conducted. The spatio-temporal dynamics of the underwater discharge was studied recording plasma images with an ICCD camera (Andor iStar DH340T-25U-03) coupled with a lens (UV-Nikkor 105 mm, f/4.5). Single-shot and accumulated images were recorded. The ICCD camera was externally triggered by the same delay generator than the HV power supply. The smallest available ICCD gate width was 3 ns. Moreover, during inter-pulses, images were recorded with back-light illumination provided by a 250 W quartz tungsten lamp (Lowel Pro-Light) to realize shadow-graphs.

For spectroscopic purposes, the light emitted at the tip of the anode was focused onto the entrance slit of a spectrometer (Andor Shamrock SR-303i, 303 mm focal length) in a 2 f-2 f configuration (no magnification) using a MgF$_2$ coated UV-near IR achromatic triplet lens (Edmund Optics, f = 90 mm). To capture the emission from the UV to the near-infrared, the spectrometer is equipped with a grating of 150 grooves mm^{-1}, blazed at 500 nm and a 50 μm entrance slit width was employed. Finally, the spectrometer is backed by the same ICCD camera used for direct imaging of the discharge (512 × 2048 pixels, 13.5 μm pixel size). The spectral resolution of the system measured with an Hg(Ar) pencil lamp (Oriel model 6035) at 546.075 nm is about 1 nm. The spatial

resolution is estimated to be about 20 μm. The absolute spectral irradiance of the plasma emission was obtained using a calibrated 200 W NIST-traceable quartz-tungsten-halogen (QTH) lamp (Oriel model 63355). The detailed calibration procedure is described below (absolute-intensity OES measurements sub-section).

2.3.1. Line broadening and electron densities determination.

As discussed in the introduction, electron densities can be determined from the Stark broadening of the emission lines. The observed experimental profiles result from the convolution of instrumental, natural, resonance, Doppler, Van der Waals, self-absorption and Stark broadening mechanisms. Table 1 summarizes the different broadening widths and associated shifts for the lines pertaining to this work (H$_\alpha$, H$_\beta$ and O(777)) as functions of the total gas pressure P, the gas temperature T_g, the electron number density n_e and the molar fraction of H and O atoms (X_H and X_O, respectively). The table is adapted (and corrected) from (Sainct *et al* 2020) and based on (Griem 1964, Gigosos *et al* 2003, Laux *et al* 2003, Bruggeman *et al* 2009, 2010, van der Horst *et al* 2012, Kielkopf and Allard 2014). It should be noted that a few simplifications were considered to obtain the formulas included in table 1. For instance, for H$_\alpha$ and H$_\beta$ Stark broadening calculations, the Stark broadening arising from hydrogen ions was neglected (compared with the electron contribution). For van der Waals calculations, water vapor was considered to be the collisional perturber. Finally, for O(777 nm), the proposed formula regarding resonance and van der Waals broadening are valid for gas temperatures up to 5 × 10^3 and 2 × 10^3 K, respectively (Laux 1993).

From the table, it is evident that the natural broadening is very much negligible compared with the instrumental broadening. At 7000 K (peak gas temperature inferred by Grosse *et al* 2020, Von Keudell *et al* 2020), the Doppler width is only about 4 × 10^{-2} nm, a factor of 25 lower than the instrumental width. Consequently, the main broadening mechanisms that will be considered in this work are pressure broadening mechanisms (van der Waals and resonance) along with the Stark broadening. It is worth noting that the resonance broadening is expected to be negligible compared with the van der Waals broadening in the case of water vapor being the dominant species in the plasma: X_H, $X_\mathrm{O} \ll 1$. The van der Waals broadening and Stark shift reported in table 1 hint at the possibility to assess the importance of the van der Waals broadening by analyzing the experimental spectral shifts of the lines of interest.

2.3.2. Absolute-intensity OES measurements.

In order to study the mechanisms responsible for the continuum radiation observed during the main voltage pulse, we use absolute-intensity calibrated OES. Such approach has been successfully employed previously in the literature to discriminate between blackbody radiation and other sources of continuum radiation (Bogen *et al* 1968, Taylor and Caledonia 1969, Frommhold 1998, Burm 2004). Absolute calibration of the

Table 1. Broadening FWHMs and shifts (in nm) for H_α, H_β and the O triplet at 777 nm, as a function of P, T, n_e, X_H and X_O. P is the pressure in bar, T the gas temperature in K, n_e the electronic density in m^{-3}, X_O and X_H are the oxygen and hydrogen mole fraction, respectively. vdW stands for van der Waals broadening. (Griem 1964, Laux 1993, Gigosos *et al* 2003, Laux *et al* 2003, Bruggeman *et al* 2009, 2010, van der Horst *et al* 2012, Kielkopf and Allard 2014, Sainct *et al* 2020).

Mechanisms (broadenings and shifts)	H_α 656.3 nm 3d→2p	H_β 486.1 nm 4d→2p	O 777 nm $^5P \rightarrow {}^5S^\circ$
FWHM (Natural)	11×10^{-5}	6.2×10^{-5}	1.1×10^{-5}
FWHM (Doppler)	$4.7 \times 10^{-4} \times T_g^{0.5}$	$3.5 \times 10^{-4} \times T_g^{0.5}$	$1.4 \times 10^{-4} \times T_g^{0.5}$
FWHM (vdW)	$5.4 \times P/T_g^{0.7}$	$4.1 \times P/T_g^{0.7}$	$2.2 \times P/T_g^{0.7}$
FWHM (Resonance)	$122 \times X_H \times P/T_g$	$60.4 \times X_H \times P/T_g$	$5.10^{-4} \times X_O \times P/T_g$
FWHM (Stark)	$8.33 \times 10^{-3} \times (n_e/10^{20})^{0.67}$	$4.80 \times (n_e/10^{23})^{0.68}$	$6.5 \times 10^{-25} \times n_e$
Shift (Stark)	$6.8 \times 10^{-2} \times (\text{Stark width})^{1.5}$		
Shift (vdW)	FWHM (vdW)/3	FWHM (vdW)/3	FWHM (vdW)/3

plasma emission was performed by replacing the discharge source in figure 1(a) with an iris (of ~1 mm diameter), image of the filament of a quartz tungsten halogen (QTH) lamp (see figure 1(d)). We implemented the different steps of the calibration procedure as detailed in (Xiong *et al* 2013, Taghizadeh *et al* 2014). Briefly, the absolute spectral irradiance of the plasma $I_{\text{Plasma},\lambda}$ in units of $W \cdot m^{-2} \cdot nm^{-1}$ at a wavelength λ can be obtained from:

$$I_{\text{Plasma},\lambda}(\lambda) = \frac{h_{\text{Plasma},\lambda}(\lambda)}{h_{\text{Lamp},\lambda}(\lambda)} I_{\text{Lamp},\lambda}(\lambda), \quad (1)$$

with $h_{\text{Lamp},\lambda}$ and $h_{\text{Plasma},\lambda}$ the measured relative emission intensities from the QTH lamp and plasma, respectively and $I_{\text{Lamp},\lambda}$ the manufacturer-provided absolute spectral irradiance of the QTH lamp in units of $W \, m^{-2} \, nm^{-1}$ provided at a distance from the source corresponding to the distance between light source and orifice. Following equation (1), the absolute plasma emissivity $\varepsilon_{\text{Plasma},\lambda}$ in units of $W \, m^{-3} \, nm^{-1}$ in a 4π steradians solid angle can be obtained from:

$$\varepsilon_{\text{Plasma},\lambda}(\lambda) = \frac{d^2}{V_{\text{Plasma}}} I_{\text{Plasma},\lambda}(\lambda), \quad (2)$$

with $d = 50$ cm, the distance between the QTH lamp filament and the iris and V_{Plasma} the volume of the plasma based on an emitting sphere of 300 μm diameter, consistently with the plasma images (see below).

2.3.3. Blackbody radiation.

Assuming that the emitting plasma is a blackbody in our observation spectral range (300–800 nm), we can replace $I_{\text{Plasma},\lambda}$ in equation (2) by the Planck analytical expression of the spectral irradiance of a blackbody at temperature T in a 4π steradians solid angle as a function of the radiating wavelength (Penner 1959, Sharkov 2003):

$$I_{BB}(\lambda) = \frac{8\pi hc^2}{n^2 \lambda^5} \frac{1}{e^{\frac{hc}{n\lambda k_b T}} - 1}, \quad (3)$$

where h, c, n and k_b denote the Planck constant, the speed of light in vacuum, the refractive index of the emitting medium and the Boltzmann constant, respectively. For our calculations, we consider $n = 1$. I_{BB} has the units of $W \, m^{-2} \, nm^{-1}$.

2.3.4. H_2 continuum radiation.

For H_2 containing plasmas, in addition to the well-known Balmer series and Fulcher-α band ($d^3\Pi_u^- \rightarrow a^3\Sigma_g^+$ around 600 nm) spectral features, it is also possible to observe the $H_2(a^3\Sigma_g^+ \rightarrow b^3\Sigma_u^+)$ dissociative continuum radiation (Lavrov *et al* 1999, Fantz *et al* 2000). From both previous observations and calculations, this continuum radiation is known to be able to extend from the far-UV (~120 nm) up to about 600 nm in the visible, with a negligible contribution above 600 nm (Fantz *et al* 2000). The intensity of the continuum depends on the vibrational population densities of the excited state $a^3\Sigma_g^+$ and on their spontaneous emission probabilities. In our experiments, H_2 molecules could be present as a result of H_2O molecules dissociation and recombination of the resulting H atoms. Assuming a population of the vibrational levels of the excited state $a^3\Sigma_g^+$ by electron-impact excitation from the ground-state $X^1\Sigma_g^+$, Fantz *et al* and Lavrov *et al* performed calculations of the absolute emissivity of the H_2 continuum radiation, as a function of the electron number density (n_e), the H_2 number density (n_{H2}), the electron temperature T_e and the vibrational temperature (T_{vib}) of the ground-state level. Instead of performing the complete calculations of absolute emissivities spectra, we will directly use the results from Fantz *et al* (see figure 2 of Fantz *et al* 2000) to obtain estimates of absolute H_2 continuum emission intensities. This is justified since the expected ionization degrees relevant to this work are large (~10^{-4}–10^{-3} (Grosse *et al* 2019, Li *et al* 2020)), electron-impact excitation is expected to be the main population mechanism for the vibrational levels of the $a^3\Sigma_g^+$ state. Conversely for ionization degrees ~10^{-7}–10^{-6} it has been demonstrated that other excitation mechanisms such as Penning ionization will be dominant (Park *et al* 2014).

2.3.5. Bremsstrahlung radiation processes.

Other candidates for the observed spectrally-broad continuum radiation include those originating from the interaction between free electrons and neutrals on one hand (electron–neutral bremsstrahlung) and between free electrons and ions on the other hand (electron–ion bremsstrahlung) (de Regt *et al* 1995). In the latter case, there is a distinction made depending on whether the electron is captured by the Coulomb field of the
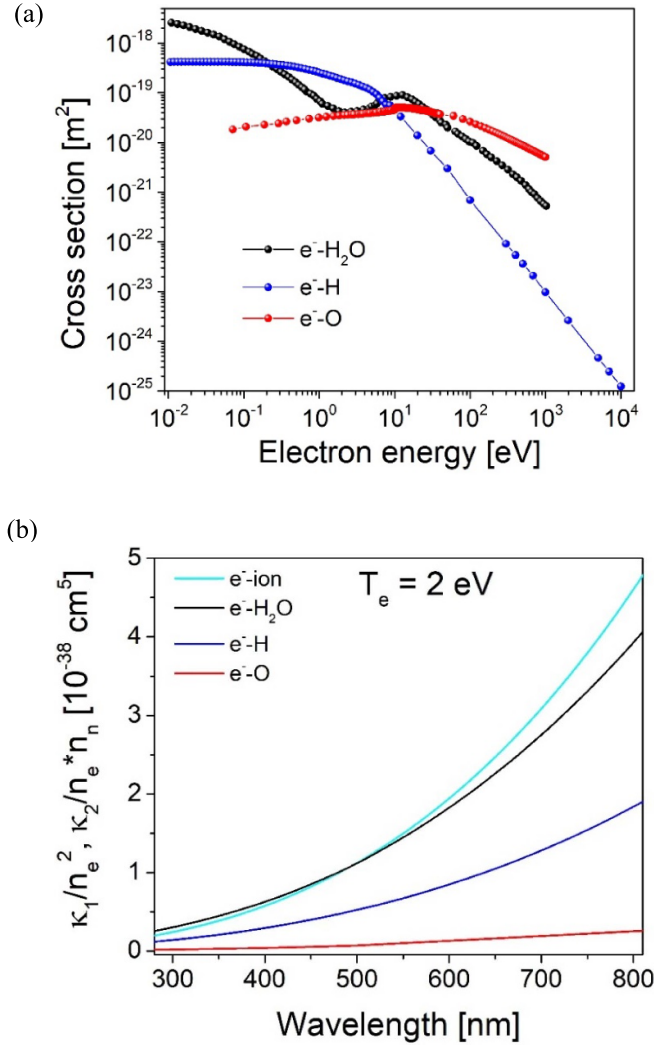
Figure 2. (a) Momentum transfer cross sections as function of the electron energy for electrons collisions with H_2O, H and O, respectively. (b) Calculated absorption coefficients for electron–ion and electron–neutrals (H_2O, H and O) inverse bremsstrahlung at $T_e = 2$ eV.

ion (free–bound radiation) or if only the electron momentum is changed by its Coulomb collision with the ion (free–free radiation) (de Regt *et al* 1995). It should be noted that following its definition, electron–neutral bremsstrahlung, which is the radiative scattering (elastic and inelastic) of electrons from neutral species only deals with free–free radiation (Taylor and Caledonia 1969, Buzulutskov *et al* 2018). The expressions of the emissivities (in W m^{-4} SI units or W m^{-3} nm^{-1}) of electron–ion free–free (ε_{ei}^{ff}), electron–ion free–bound (ε_{ei}^{fb}), electron–neutral free–free (ε_{en}) and total continuum (ε_{cont}) radiations are as follows (Wilbers *et al* 1991, Burm 2004, Park *et al* 2014):

$$\varepsilon_{ei}^{ff} = 4\pi \ C_{ei} \ \zeta_{ei}^{ff} \ \frac{n_e n_i}{\lambda^2} \ \frac{c}{\sqrt{k_b T_e}} \mathrm{e}^{-\frac{hc}{\lambda k_b T_e}}, \tag{4}$$

$$\varepsilon_{ei}^{fb} = 4\pi \ C_{ei} \ \zeta_{ei}^{fb} \ \frac{n_e n_i}{\lambda^2} \ \frac{c}{\sqrt{k_b T_e}} \left[1 - \mathrm{e}^{-\frac{hc}{\lambda k_b T_e}} \right], \tag{5}$$

$$\varepsilon_{en} = 4\pi \ C_{en} \ \frac{n_e n_n}{\lambda^2} \ \frac{1}{(k_b T_e)^{3/2}} \int\limits_{\frac{hc}{\lambda}}^{\infty} Q_{en}^{mom} (E) \left(1 - \frac{hc}{2\lambda E} \right)$$

$$\times \sqrt{1 - \frac{hc}{\lambda E}} \mathrm{e}^{-\frac{E}{kT_e}} E^2 \mathrm{d}E, \tag{6}$$

$$\varepsilon_{cont} = \varepsilon_{ei}^{ff} + \varepsilon_{ei}^{fb} + \varepsilon_{en}, \tag{7}$$

with $C_{ei} = \frac{1}{(4\pi\varepsilon_0)^3} \frac{32\pi^2 e^6}{3\sqrt{3}c^3 (2\pi m_e)^{3/2}} \simeq 2.03 \times 10^{-63}$ J$^{3/2}$ m^3 sr^{-1} and $C_{en} = \frac{4\sqrt{2}}{3\pi^{5/2}} \frac{\alpha h}{m_e c} \simeq 2$ W m^2 J$^{-3/2}$ sr^{-1}. Where n_e, n_i, λ, T_e, n_n, E, e, ε_0, m_e and α are the electron number density, the ion number density, the emitted photon wavelength, the electron temperature, the neutral number density, the electron energy, the elementary charge, the vacuum permittivity, the electron mass and the fine structure constant, respectively. ζ_{ei}^{ff} and ζ_{ei}^{fb} are the free–free and free–bound Biberman factors accounting for non-hydrogenic behavior of the radiation levels of the gas (Burm 2004). Q_{en}^{mom} is the electron–neutral collision momentum transfer cross-section.

It is important to note that equations (4)–(6) are obtained using a few assumptions: (1) a Maxwellian electron energy distribution function and (2) a singly-ionized plasma. Further, to perform the calculations of the different aforementioned contributions, we assume (3) a quasi-neutral plasma ($n_i = n_e$) and (4) the wavelength-dependent free–free and free–bound Biberman factors are equal to 1 between 300 and 800 nm (Wilbers *et al* 1991, de Regt *et al* 1995). While ε_{ei}^{ff} and ε_{ei}^{fb} are both proportional to n_e^2 and ε_{en} is proportional to $n_e \times n_n$. Finally, we use electron–neutral momentum transfer cross-sections considering H_2O, H, O (and their mixtures) as the neutral species interacting with the electrons. When dealing with mixtures of different species, the expressions of electron–ion free–bound and free–free emissivities (equations (4) and (5)) remain unchanged. However, in first order approximation, the total electron–neutral momentum transfer cross-section is the weighted-average of the different electron–neutral momentum transfer cross-sections for each species:

$$n_n Q_{en}^{mom} = n_1 Q_{e-sp1}^{mom} + n_2 Q_{e-sp2}^{mom} + \ldots + n_m Q_{e-spm}^{mom}$$

$$= n_n \left(\frac{n_1}{n_n} Q_{e-sp1}^{mom} + \frac{n_2}{n_n} Q_{e-sp2}^{mom} + \ldots + \frac{n_m}{n_n} Q_{e-spm}^{mom} \right), \tag{8}$$

where n_1, n_2 and n_m are the densities of neutral species 1, 2 and m, respectively. n_n is the total neutral density. Q_{e-sp1}^{mom}, Q_{e-sp2}^{mom} and Q_{e-spm}^{mom} are the electron–neutral momentum transfer cross-sections for species 1, 2 and m, respectively in units of m^2.

The cross-sections data as functions of the electron energy were taken from (Itikawa 1974, Itikawa and Ichimura 1990, Itikawa and Mason 2005) for electron energies up to 100, 10 and 12 eV, respectively. At high electron energies up to 10^3–10^4 eV, the previous data was complemented using cross-sections sets from Hayashi (Hayashi 1987) and IST-Lisbon (Mukherjee *et al*, 1987, Laher and Gilmore 1990, Bray *et al* 1991) retrieved from the LXCat database (Pitchford

et al 2017). A special care was taken to ensure a smooth continuity between cross-section sets. The resulting compiled cross-sections as functions of the electron energy are plotted in figure 2(a). On a separate note, we do not discuss the contributions of the polarization bremsstrahlung, which is considered to be relevant starting from keV electron energies (Buzulutskov *et al* 2018) and of electron–electron collisions, which are only relevant for the cases of relativistic electrons (few MeV electron energies) (Hutchinson 2002). Such high electron energies are for instance encountered in laser-produced plasmas with power densities above 10^{20} GW cm^{-2} (Bulanov *et al* 2010), many orders of magnitude above the power densities relevant to this work.

2.3.6. Model for self-absorption. In order to account for the attenuation of the emitted radiation due to self-absorption, we apply the model described in (François 1974), valid for spherical emitters:

$$\frac{J}{J_0} = \frac{3}{4(\mu R)^3} \left[(\mu R)^2 - \frac{1}{2} + \left(\mu R + \frac{1}{2} \right) e^{-2\mu R} \right], \quad (9)$$

where J, J_0, μ and R denote the radiation emitted by the spherical source, the radiation emitted by the source if there was no self-absorption, the attenuation (absorption) coefficient and the source radius, respectively. We consider both electron–ion free–free inverse bremsstrahlung and electron–neutral free–free inverse bremsstrahlung as attenuation processes.

The electron–ion free–free inverse bremsstrahlung spectral absorption coefficient $\kappa_1(\lambda)$ (in units of m^{-1}) is given by the Kramers equation (Zel'dovich and Raizer 1966, Khalid *et al* 2012):

$$\kappa_1(\lambda) = \frac{n_e^2 \lambda^3}{C_1 \sqrt{T_e} c^3}, \quad (10)$$

where $C_1 = \frac{\sqrt{3 m_e k_b} 3 h c m_e (4\pi\varepsilon_0)^3}{4\sqrt{2\pi} e^6} \simeq 27.24$ m^{-5} s^3 K$^{-0.5}$. Consistently with equation (4), in equation (10) we assumed (1) $n_e = n_i$ (2) singly-charged positive ions ($Z = 1$) and (3) a Maxwellian EEDF. It is important to point out that $\kappa_1(\lambda)$ is proportional to $n_e^2 \times \lambda^3$ and inversely proportional to $T_e^{0.5}$. This means that the opacity effects related to electron–ion free–free interactions are expected to be more preponderant at large n_e, larger wavelengths and for low T_e values.

The absorption coefficient for electron–neutrals inverse bremsstrahlung $\kappa_2(\lambda)$ is discussed by (Geltman 1965, 1973, Mjolsness and Ruppel 1967, Chauveau *et al* 2003). Advanced and detailed calculations regarding electron-atom and electron-molecule inverse bremsstrahlung absorption coefficients for species such as H, O, N and N$_2$ were provided in the literature by the previously mentioned authors. In practice, data from the literature are often tabulated as $\kappa_2(\lambda) / (n_e \times n_n)$ in units of m^5 or cm^5. We employed the data provided by Geltman for H and O (Geltman 1973) and extended it to lower photon wavelengths and specific T_e values using the analytical expression provided by equation (4) in (Mjolsness

and Ruppel 1967). Since to the best of our knowledge, e$^-$ H$_2$O free–free absorption cross-section data is not available in the literature, we assumed that the corresponding absorption coefficient is equal to the sum of the absorption coefficients of its atomic constituents. Such approximation has been previously employed in the literature (Hammer and Frommhold 2002) and we will show that it does not significantly affect the end results (a factor of 2 difference at most). Figure 2(b) shows the calculated $\kappa_1(\lambda) / (n_e^2)$ and $\kappa_2(\lambda) / (n_e \times n_n)$ as functions of the absorbed photon energy between 300 and 800 nm, for $T_e = 2$ eV and for e$^-$ O, e$^-$ H and e$^-$ H$_2$O, respectively.

Finally, it is important to point out that we neglected the photo-ionization of ions (bound–free electron–ion absorption) in order to stay consistent with singly-charged ions. The photo-ionization of neutral species was also neglected since a 300 nm wavelength-light emitted by the plasma only corresponds to ~4.13 eV < 11.2 eV, 12.6 eV. 11.2 eV and 12.6 eV are the ionization energies of liquid water and water vapor, respectively. Multiphoton (3 or more photons) absorption would hence be needed from the ground state. But because water features a weak absorption in the near UV (above 200 nm) and visible spectral ranges, photoionization is unlikely to occur.

3. Results and discussion

Figure 3(a) shows the recorded voltage and current waveforms using D-dot and B-dot probes, respectively for a 40 kV applied voltage at 10 Hz pulse repetition frequency. The measurements show that both waveforms consist of wave trains extending up to 4 μs after the onset of the applied voltage. The discharge voltage and current peak at 55 kV and 50 A, respectively during the 10 ns main voltage pulse. The main voltage pulse is followed by lower amplitude voltage pulses separated by about 200 ns each, corresponding to reflections in the transmission line. These reflections arise from the impedance mismatch between the transmission line and the load (the plasma discharge). It should be noted that the observed 200 ns time separation is consistent with the distance traveled back and forth (two cable lengths i.e. 40 m) and the speed of the electrical signal in the coaxial cable (about 2 × 10^8 m·s^{-1}). Interestingly from figure 3(b), even though the peak coupled power occurs during the main voltage pulse (peaking at about 3.5 MW), the coupled energy by reflections accounts for half of the total ~70 mJ coupled energy. This is a key finding of our work since previous works have mostly only quantified the coupled energy during the first pulse (see for instance Marinov *et al* 2014). More detailed, substantial power coupling occurs during the main voltage and then at $t = 550$, 760 and 970 ns.

Figure 4 shows the spatio-temporal dynamics of the discharge using single-shot ICCD images. The timing indicated beneath each image is made consistent with that of figure 3. From the images, it appears that during the main voltage pulse,
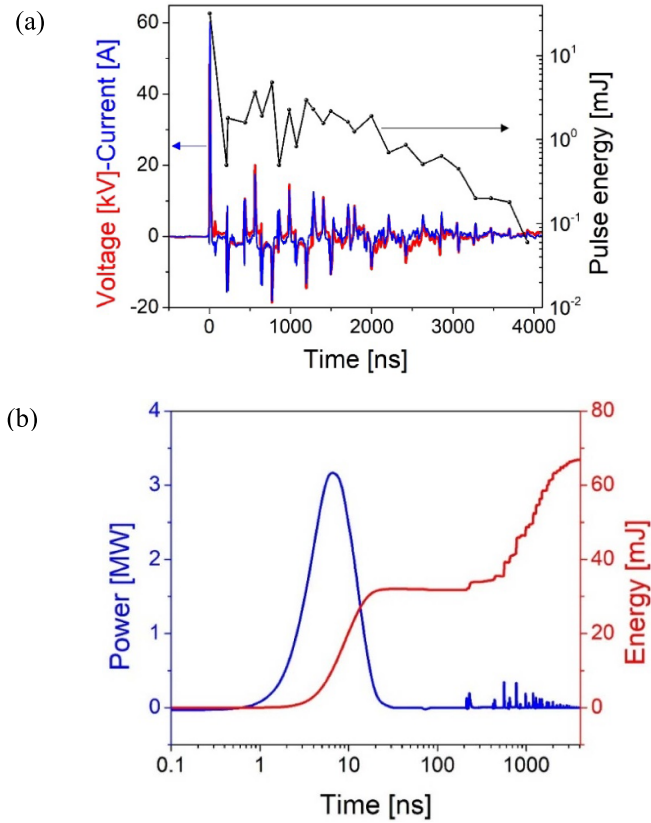
(a)

(b)

Figure 3. (a) Voltage and current waveforms obtained from D-dot and B-dot probes at 40 kV applied voltage. (b) Coupled power and energy waveforms. The pulse repetition frequency and water conductivity are 10 Hz and 250 μS cm^{-1}, respectively.

the discharge has a corona-like morphology (spherical shape with a characteristic diameter of about 300 μm) and is located right at the tip of the HV electrode. The location of the pin is evident from the shadow-graph images on the right side. During the subsequent reflected pulses, we can see that the discharge becomes filamentary with a stochastic, streamer-like structure. When using larger gate widths (30 ns to 500 ns), it is evident that the filaments can reach millimeter lengths (up to about 2 mm). Furthermore, the filaments are found to be relatively thin, exhibiting streamer-like channels with a characteristic width of about 150 μm. From the shadow-graph images, we remark that clusters of bubbles are generated in between pulses. In addition, the discharges during the reflected pulses seem to follow the path traced by the bubbles. This suggests that the filamentary discharges are generated in the immersed water vapor bubbles in the liquid and hence in the gas phase. These findings are consistent with those reported by (Pongrác *et al* 2018, Grosse *et al* 2019). Because degassing of the liquid was not performed during the experiments, we cannot exclude the possibility that the discharge during the main voltage pulse might be affected by leftover microscopic bubbles from the previous discharge pulse (see Simek *et al* 2020a for instance). Interestingly, if we consider that the peak power of 3.5 MW is dissipated in a 7×10^{-4} cm^2 area (300 μm diameter sphere), the power density obtained $\sim$5 GW cm^{-2} is

interestingly comparable to that of 10 ns duration CO$_2$ lasers emitting at 10.6 μm for the generation of EUV light at 13.5 nm using tin droplets (Banine *et al* 2011). Moreover, from the measured peak voltage (50 kV) and the pin radius of curvature $\sim$100 μm, the peak Laplacian field obtained at the tip of the pin and estimated using equation (4) of (Seepersad *et al* 2013b) is about 1.3 MV cm^{-1}. This value is high enough to generate voids through the electrostrictive force for a fast-rising voltage pulse (Seepersad *et al* 2013a).

Figure 5 displays the temporal evolution of the relative plasma emission spectra near the tip of the anode. These spectra were spatially averaged over the entire discharge cross section following the implementation of pixel binning during data processing. A 50 ns camera gate along with 50 accumulations was used for the main voltage pulse whereas 100 ns gate widths and 1000 accumulations were used for each reflected pulse. We observe that the plasma emission is clearly overall dominated by the emission of the first pulse. Furthermore, during the first pulse a broad continuum emission spanning from the UV to the near-infrared is observed. No molecular bands nor atomic emission lines are present, in contrast with the following reflected pulses for which signatures of atomic and molecular species are evidenced. Although 3 ns time-resolved spectra were recorded during the main voltage pulse, the shape of the spectra did not vary on this timescale and were identical to that of the 50 ns time-resolved one depicted in figure 5. We therefore focused our analysis on the latter spectrum. H$_\alpha$ (656.3 nm), H$_\beta$ (486.1 nm), H$_\gamma$ (434 nm), O (777 nm), Na (589 nm) and OH (306 nm) (first and second diffraction orders) are visible in the spectra of figure 5. A peak FWHM of about 14 nm is measured for the H$_\beta$ transition at $t = 760$ ns. H$_\alpha$ emission dominates the lines intensities over the entire span of the discharge, followed by O (777 nm) and H$_\beta$. Interestingly, von Keudell *et al* (2020) did not observe OH (A $^2\Sigma^+ \to$ X $^2\Pi$) emission.

Assuming that Stark broadening is the dominant broadening mechanism for the α and β transitions of the Balmer series and for the O (777 nm) line, we can infer the temporal evolution of the discharge electron densities during the reflected pulses. The results are depicted in figure 6. One could note that the intensity of the Balmer γ transition is too weak to be employed for any spectroscopic purposes. As discussed earlier, the previously mentioned assumption is justified by the negligible natural, Doppler and instrumental broadenings compared with the measured widths of the atomic lines investigated. It is well-known that the gas pressure can reach values up to GPa during the main voltage pulse. However, the slowest pressure relaxation time based on the diameter of the spherical discharge (300 μm) and considering underwater acoustic waves traveling at the sound speed at 300 K ($\sim$1500 m s^{-1}) is estimated to be about 200 ns. This result hints that the gas pressure during the filamentary discharges (starting at $t = 210$ ns) is not as high as that of the spherical discharge generating the intense continuum radiation. This is further supported by the fact that no spectral shift of the atomic lines was observed (within the instrument spectral resolution). We can hence neglect the Van der Waals broadening mechanism for
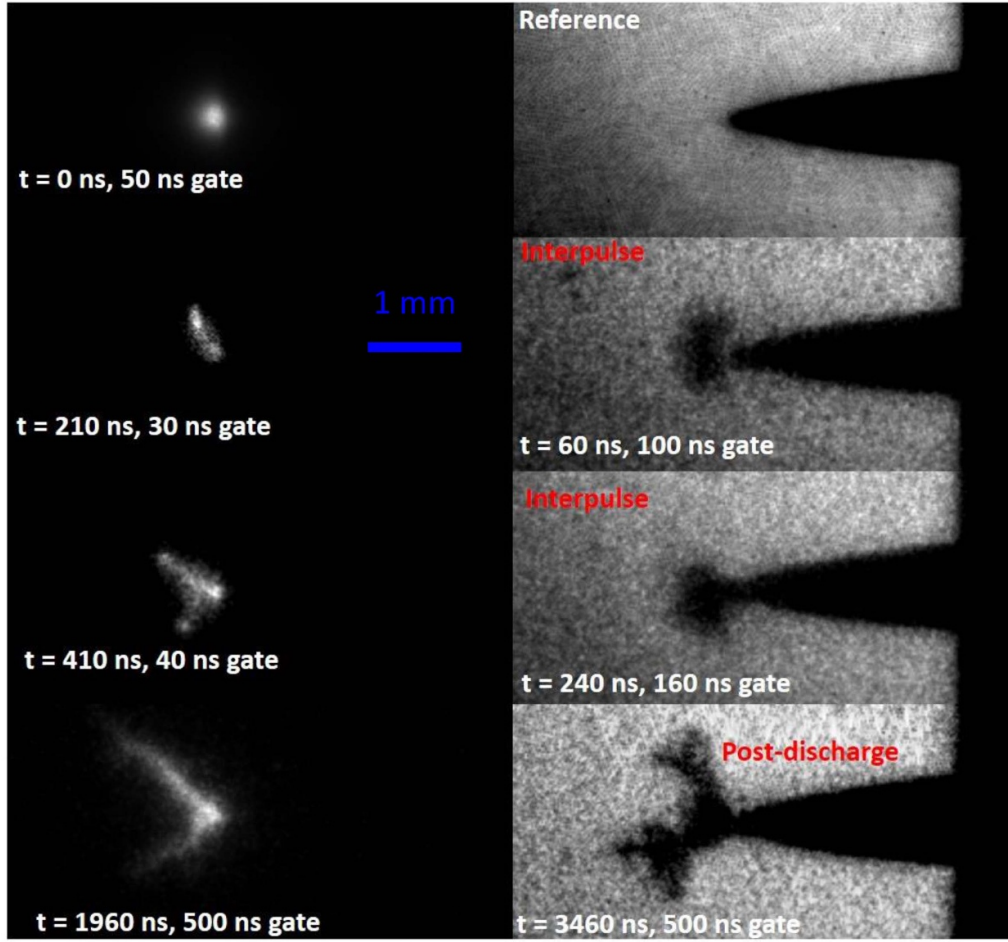
Figure 4. Single-shot broadband plasma images and shadow-graphs taken at different moments in time during the main voltage pulse, interpulses, secondary voltage pulses and post-discharge. The camera gate duration is indicated for each image. The reference image shows the location of the tungsten pin.
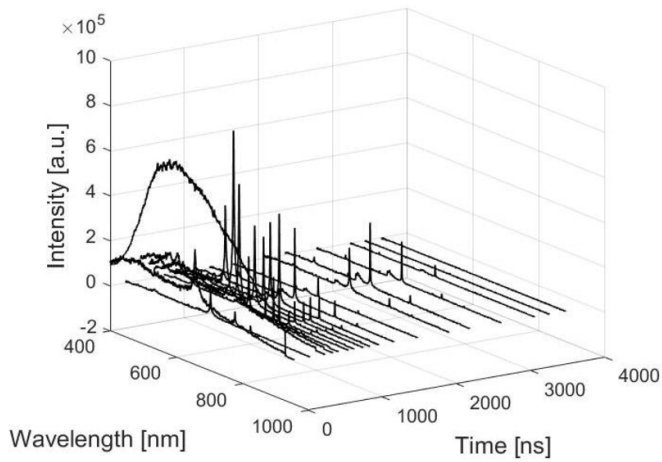

Figure 5. Temporal evolution of the broadband emission spectra during the discharge. Main voltage pulse: 50 ns camera gate and 50 accumulations. Secondary voltage pulses: 100 ns gate and 1000 accumulations.

the reflected pulses. Also, based on table 1 a negligible Van der Waals broadening implies a negligible resonance broadening, if we assume $X_{O,H} \ll 1$. Figure 6 shows that the peak measured

electron number density for the streamer-like discharges is about 3×10^{24} m^{-3}, occurring during the first reflected pulse at $t = 210$ ns. Following the first reflected pulse, the plot n_e versus time displays an overall exponentially decreasing trend, only perturbed by punctual increases of n_e when energy is coupled in by other reflected pulses. This is especially visible at $t = 550$ ns, 760 ns for which relatively high-energy values are coupled to the discharge (see figure 3(b)) and higher n_e values are observed giving rise to the observed damped sawtooth-like structure. The lowest n_e measured is about 5×10^{22} m^{-3}, at $t \approx 2800$ ns showing a decrease of the electron number density by almost two orders of magnitude over 3 μs. The error bars displayed in figure 6 arise mostly from the uncertainty estimate from background subtraction and by comparing single-shot and time-averaged data. Within these error bars, results inferred from H$_\alpha$ and O (777 nm) seem to be in good agreement and consistently higher than results obtained from H$_\beta$ Stark broadening. Many reasons could explain such outcome: (1) the sensitivity of the FWHM of H$_\alpha$ to the ions dynamics (ion-motion effect) (Nikiforov *et al* 2015) that was neglected for the Stark broadening calculations, (2) the sensitivity of the H$_\alpha$ profile to self-absorption, resulting in the broadening of the spectral feature (Bruggeman *et al* 2009) and (3) the sensitivity
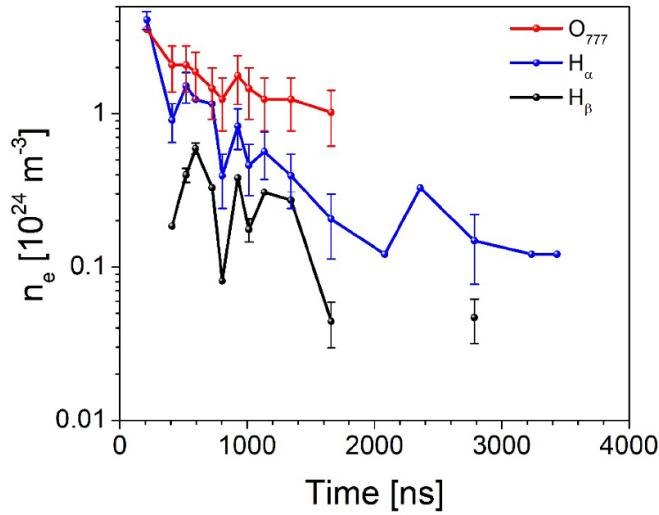
Figure 6. Time-resolved electron densities inferred from the stark broadenings of H_α, H_β and O_{777} lines.

Figure 7. Comparison of the main voltage pulse and blackbody (BB) assuming 0.80, 0.82 and 0.85 eV on an absolute scale in term of emissivity using the quartz tungsten-halogen lamp. The peak around 730 nm in the plasma emission spectrum is an artifact of the absolute calibration.

of the H_β Stark width to the gas temperature for temperatures higher than ~1 eV (Konjevic *et al* 2012).

Figure 7 displays the absolute experimental plasma emissivity together with the corresponding absolute blackbody emissivity calculated for $T = 0.80–085$ eV (we considered $n = 1$). Similarly to previous results from (Grosse *et al* 2020), figure 7 shows that the shape of the spectral-corrected experimental plasma emissivity is very similar to that of a blackbody at temperatures up to ~9.3–9.9 × 10³ K. However, when compared on an absolute scale, it is clear that the expected intensity from a blackbody at such high temperature is over seven orders of magnitude higher than the experimentally measured absolute radiation. Consequently, we can conclude that blackbody radiation cannot be responsible for the measured continuum emission. Still, the observed emission would match that of a grey-body under the assumption of a very low, wavelength-independent relative spectral emissivity of the plasma. However, there is no physics-based argument to support such an assumption. In fact, similar conclusions were drawn by (An 2006) for sonoluminescence. Interestingly, if we assume that 1%–10% of the entire $P = 3.5$ MW power coupled in during the main voltage pulse is radiated by a spherical blackbody of 300 μm diameter, based on the Stefan–Boltzmann law (Penner 1959) we get a temperature ranging from 5.4 × 10⁴ K to 9.7 × 10⁴ K (~5 eV–8 eV). $P = \sigma_{SB} \times T^4 \times A$, σ_{SB} is the Stefan–Boltzmann constant and A is the area of the radiating sphere. This, of course constitutes an upper limit of the temperature that could be attained in our system. In case of a non-ideal blackbody radiation, radiation losses other than thermal radiation will cause a significant temperature drop.

3.1. Fitting of the main voltage pulse

Before fitting the experimental data with bremsstrahlung calculations, we can perform a rough estimate of the maximum
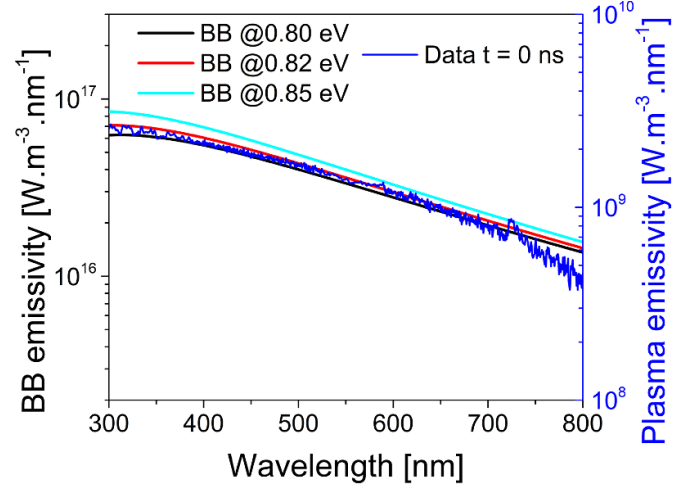
electron density that can be attained during the main voltage pulse. Suppose we consider T_e in the range of 2–5 eV, which is typical for pulsed nanosecond discharges containing large amount of water vapor at atmospheric pressure (Luo *et al* 2019). If in addition we assume a Maxwellian EEDF, based on Bolsig+ calculations (Hagelaar and Pitchford 2005) the fraction γ of the input energy electron energy going into the ionization channel can be obtained. We find $\gamma = 0.1\%, 2\%, 10\%$, and 20% for T_e values of 2, 3, 4 and 5 eV, respectively. The total energy required for a single ionization is $\varepsilon_{ioni}/\gamma$ with ε_{ioni} the ionization energy of water. We can thus infer the number of ionization events and thereafter the electron number density as a function of the total input energy ε_T and plasma volume V_{Plasma}:

$$n_{e,max} = \frac{\gamma \epsilon_T}{\epsilon_{ioni} V_{Plasma}}, \tag{11}$$

with $\varepsilon_T = 35$ mJ ~ 2.19 × 10¹⁷ eV, $\varepsilon_{ioni} = 12.6$ eV and $V_{Plasma} = 1.4 × 10^{-11}$ m³. For 2 eV $\leqslant T_e \leqslant$ 5 eV, we find 10^{24} m⁻³ $\leqslant n_{e,max} \leqslant$ 3 × 10²⁶ m⁻³ and a monotonic increase in the maximum electron density with the increase of the electron temperature. Assumptions made to obtain these results are summarized as: (1) dense gas approximation, (2) Maxwell-Boltzmann EEDF and (3) ionization energy equal to that of water vapor (12.6 eV). Additionally, it is also assumed there is no electron loss process on these time scales and that ionization takes place through single ionization processes (for example electron-impact ionization). Among the above assumptions, the dense gas approximation is expected to be the most impactful on our analysis since it does not incorporate effects of the surrounding liquid medium as well as strong coupling and collective effects between particles in a dense plasma.
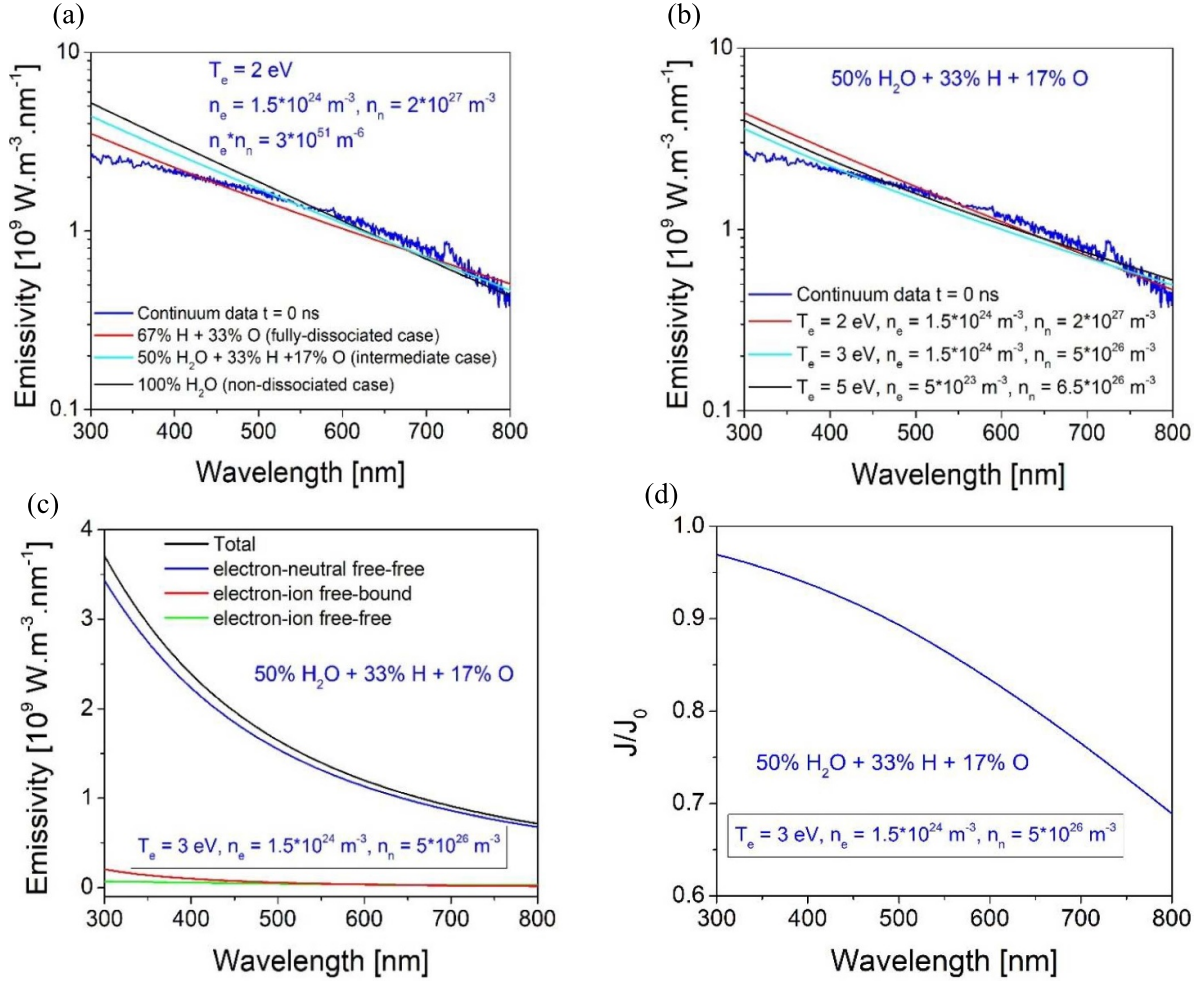
Figure 8. (a) Measured main voltage pulse absolute emissivity together with total bremsstrahlung (emission and absorption) fits for three different mixtures composition at $T_e = 2$ eV. (b) Bremsstrahlung fits for the intermediate mixture case for different T_e values. (c) Components of the bremsstrahlung emission for $T_e = 3$ eV and for the intermediate mixture case. (d) Emission intensity reduction due to self-absorption effects for $T_e = 3$ eV and for the intermediate mixture. The peak around 730 nm in the plasma emission spectrum is an artifact of the absolute calibration.

The fitting results (with self-absorption effects accounted for) of the main voltage pulse spectrum are displayed in figure 8 and consistent with the lower end of the above electron density estimate. Figure 8(a) shows fitting results at $T_e = 2$ eV for three different mixture compositions: (1) fully-dissociated case (67% H + 33% O), (2) intermediate case (50% H_2O + 33% H + 17% H) and (3) non-dissociated case (100% H_2O). A good agreement between the computed fits and the experimental data was obtained for wavelengths in excess of 500 nm for $n_e = 1.5 \times 10^{24}$ m^{-3} and $n_n = 2 \times 10^{27}$ m^{-3}. Below 500 nm, the calculations overestimate the emissivity. Interestingly, irrespective of the mixture composition, the absolute intensity of the experimental data can be matched. Figure 8(b) shows the best fits obtained for 2 eV $\leqslant T_e \leqslant$ 5 eV for the intermediate case of mixture composition. A somewhat better fit is obtained for $T_e = 3$ eV, $n_e = 1.5 \times 10^{24}$ m^{-3} and $n_n = 5 \times 10^{26}$ m^{-3}. Still, the overestimation in the lower wavelength part of the spectrum is present. This could be due to the assumption of a Maxwellian

EEDF. In fact, Nayak *et al* demonstrated that using a non-Maxwellian EEDF would likely lead to a decrease in intensity in the UV part of the continuum spectrum (2021). In our case, emissivity calculations assuming non-Maxwellian EEDFs could not be carried out because analytical expressions for self-absorption coefficients are only available for a Maxwellian EEDF. The different bremsstrahlung emission components (electron–ion free–free, electron–ion free–bound and electron–neutral free–free) of the selected fit are depicted in figure 8(c). The dominant emission mechanism is electron–neutral free–free bremsstrahlung, with a minor contribution of electron–ion free–bound bremsstrahlung emission. This is consistent with the relative high ionization degree (3×10^{-3}) and high T_e (3 eV). Finally, the self-absorption effects on the intensity of the radiated continuum are shown in figure 8(d). We observe that only about 3% of the emitted radiation is absorbed at 300 nm. This number drastically increases to about 30% at 800 nm, as a consequence of the increasing opacity with increasing absorbed photon wavelength. This might
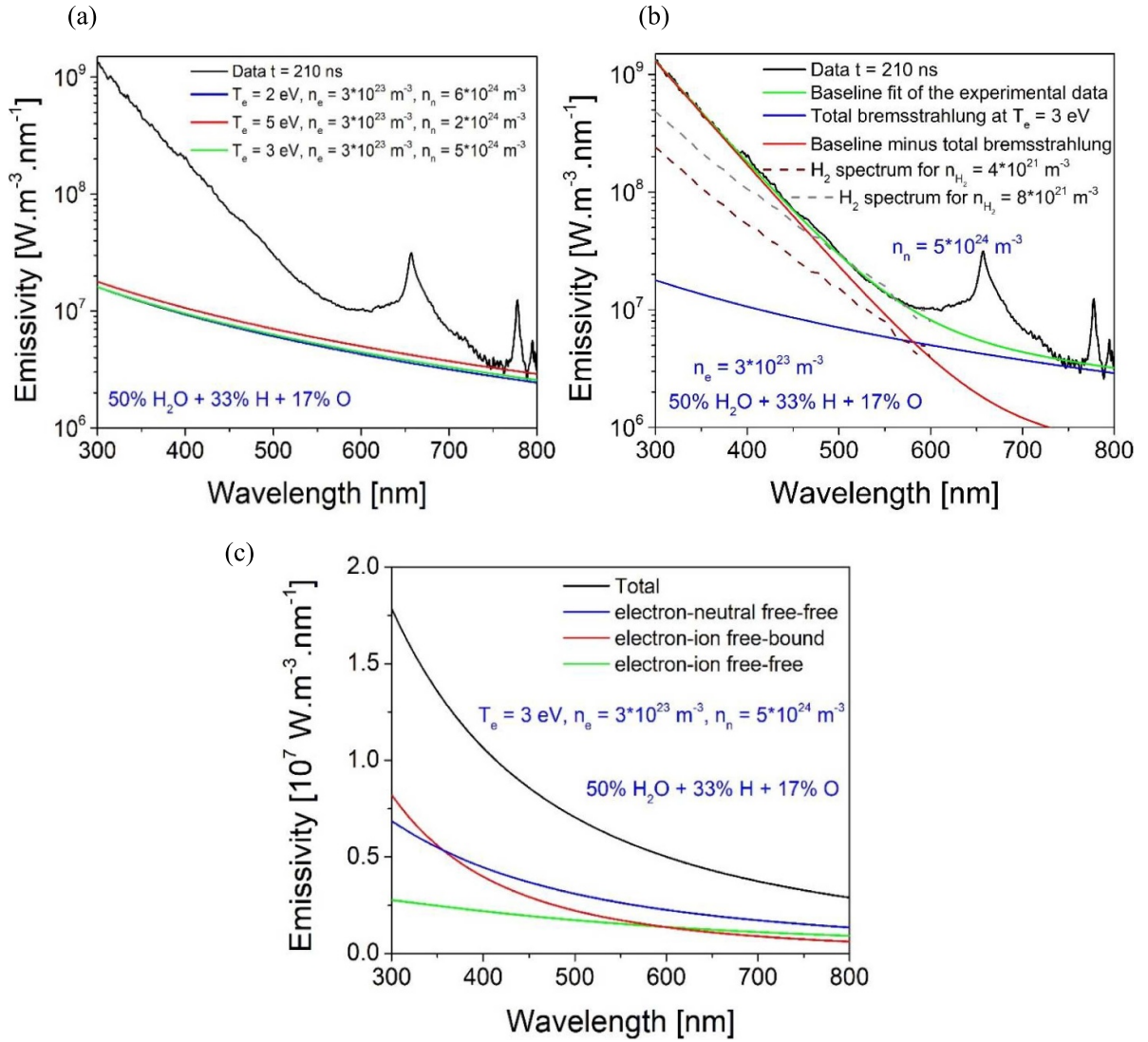
(a)

(b)

(c)

Figure 9. (a) Absolute emissivity of the second voltage pulse absolute emissivity together with total bremsstrahlung fit. (b) Measured second voltage pulse emissivity together with the best bremsstrahlung fit and sample H_2 absolute emissivity spectra for $n_{H2} = 4 \times 10^{21}$ m^{-3} and $n_e = 3 \times 10^{23}$ m^{-3}. (c) Components of the bremsstrahlung for the best fit.

suggest that more advanced self-absorption models might enable a more accurate prediction of the UV part of the continuum emission as well.

3.2. Fitting of the second voltage pulse

The second voltage pulse (or first reflection of the main voltage pulse) is of great interest because it shows overlapping continuum and line radiation features. It hence provides an opportunity to validate our continuum emission analysis approach while inferring additional plasma parameters. The fitting results of the emissivity of the secondary voltage pulse are pictured in figure 9. Figure 9(a) displays the results of the fit for the intermediate mixture case and for 2 eV $\leqslant T_e \leqslant 5$ eV considering only bremsstrahlung as emission mechanism (with self-absorption effects accounted for). Unlike figure 8(a), bremsstrahlung emission alone is not able

to reproduce the shape of the measured experimental spectrum. However, there seems to be an asymptotic agreement in the near-infrared part of the spectrum (700–800 nm). When scanning the parameter ranges 2 eV $\leqslant T_e \leqslant 5$ eV, and 10^{22} m$^{-3} \leqslant n_e \leqslant 10^{24}$ m^{-3}, the best overall near-IR agreement was obtained for $n_e = 3 \times 10^{23}$ m^{-3}, $T_e = 3$ eV and $n_n = 5 \times 10^{24}$ m^{-3}. These results were obtained when considering that the near-IR asymptotic contribution of the overall spectrum arose from Bremsstrahlung emission (see figure 9(a)) while the UV-visible part from 300 to 600 nm was dominated by the H_2 continuum spectrum (see figure 9(b)). H_2 production by underwater plasmas is well established. See for instance (Kierzkowska-Pawlak *et al* 2019, Wang *et al* 2021). Additionally, H_2 Fulcher emission has been observed for direct discharges in liquid water (Bruggeman *et al* 2009). n_e, n_n and T_e values were inferred from the Bremsstrahlung fit while n_{H2} was inferred from the addition of an H_2 continuum fit in

the UV–visible spectral range. Because full pressure relaxation is expected to have already occurred at $t = 210$ ns, a gas density of $n_n = 5 \times 10^{24}$ m^{-3} would correspond to an atmospheric pressure gas with a characteristic translational temperature of $T_g \sim 1470$ K. The inferred n_e value from the bremsstrahlung asymptotic fit is about one order of magnitude lower than the results from H$_\alpha$ and O (777 nm) Stark broadenings. However, H$_\alpha$ and O (777 nm) are known to be prone to self-absorption broadening in dense plasmas. Despite the fact that H$_\beta$ is not readily observed during the second voltage pulse (at $t = 210$ ns), at later timescales the electron density determined from the H$_\beta$ Stark broadening is up to a factor 5 lower than from H$_\alpha$ Stark broadening, suggesting indeed that H$_\alpha$ Stark broadening leads to a significant overestimation of n_e. Moreover, with the addition of H$_2$ continuum radiation for $n_{H2} = 8 \times 10^{21}$ m^{-3} and $n_e = 3 \times 10^{23}$ m^{-3}, the magnitude of the experimental UV continuum radiation spectrum can be matched (see figure 9(b)). This strongly suggests that the measured spectrum could be in fact a combination of bremsstrahlung and H$_2$ continuum. Regarding the components of the bremsstrahlung emission, from figure 9(c), it is evident that despite the dominant contribution of electron–neutral free–free bremsstrahlung, electron–ion free–bound continuum is not negligible. In fact, for $T_e = 2$ eV, electron–ion free–bound bremsstrahlung becomes dominant. As the plasma density is significantly lower than in the first pulse, self-absorption effects are negligible for this case. While the addition of H$_2$ continuum emission can explain the observed spectrum, we recognize the uncertainty in the Biberman factors that could particularly impact the shape of the observed spectrum in the UV to near-visible spectral range.

4. Conclusions

In this work we studied an underwater nanosecond pulsed discharge for a 40 kV input pulse of 10 ns duration at 10 Hz in a 250 μS cm^{-1} NaCl-distilled water solution. For our conditions, the total energy deposited is about 70 mJ. We showed that 50% of the energy coupling occurs during the secondary discharges, which last up to 4 μs after the primary discharge. During the main voltage pulse resembling a corona-like discharge, a peak power of 3.5 MW corresponding to a power density of 5 GW cm^{-2} was measured. Such high-power deposition is accompanied with continuum radiation that was investigated using absolute-intensity OES. We showed that the shape and absolute intensity of the observed continuum radiation can be explained by emission and absorption bremsstrahlung processes (electron–ion free–free, electron–ion free–bound, electron–neutral, inverse electron–ion free–free and inverse electron–neutral). The inferred electron number density and temperature values from the continuum radiation calculations for the main voltage pulse are about 10^{24} m^{-3} and 3 eV, respectively.

During the multiple secondary discharges, corresponding to streamer-like discharges and propagating in water vapor bubbles, the peak power deposited was only about 0.3 MW.

Conversely to the main voltage pulse, line emission (bound–bound radiation) was observed. We showed that Stark broadening is the dominant broadening mechanism for the observed atomic lines, since no significant spectral shifts were observed. Electron number densities were inferred from the linewidths ranging from about 4×10^{22} m^{-3}–10^{24} m^{-3}.

Interestingly, during this first secondary pulse we observed a superimposition of lines and continuum emissions. We demonstrated that in addition to bremsstrahlung processes, H$_2$ continuum radiation for a H$_2$ density ~ 0.6–1×10^{22} m^{-3} could explain the measured continuum emission in the UV–visible range (300–600 nm) of the spectrum. The electron density and electron temperature inferred from the fit of the continuum with bremsstrahlung are 3×10^{23} m^{-3} and 2–3 eV, respectively. We also found self-absorption to be negligible in that case, consistent with a lower gas density (pressure).

The results discussed in this paper are based on several approximations and simplifications that allowed us to perform estimates based on analytical calculations. Therefore, more refined radiation models and calculations provide an opportunity to improve the accuracy of the present estimation methods. Moreover, direct measurements of n_e, T_e during the main voltage pulse combined with detection and absolute density measurements of H$_2$ in the streamers using independent spectroscopic techniques present a formidable challenge for future endeavors. It is worth noting that the plasma conditions reported in this work have similarities with laser-produced plasmas used for the purposes of EUV lithography. For the latter, time-resolved Thomson scattering measurements of n_e and T_e upon impact of a CO$_2$ laser on a micro-droplet of molten tin were obtained (Tomita *et al* 2015, 2017).

Data availability statement

All data that support the findings of this study are included within the article (and any supplementary files).

ORCID iDs

Marien Simeni Simeni ⓘ https://orcid.org/0000-0002-2241-5739
Peter J Bruggeman ⓘ https://orcid.org/0000-0003-3346-7275

References

An W, Baumung K and Bluhm H 2007 Underwater streamer propagation analyzed from detailed measurements of pressure release *J. Appl. Phys.* **101** 053302

An Y 2006 Mechanism of single-bubble sonoluminescence *Phys. Rev.* E **74** 26304–18

Babický V, Člupek M and Lukeš P 2017 Determination of electrical characteristics of nanosecond discharge in liquid *19th IEEE Int. Conf. on Dielectric Liquids (ICDL2017) (Manchester, UK)* pp 1–4

Banine V Y, Koshelev K N and Swinkels G H P M 2011 Physical processes in EUV sources for microlithography *J. Phys. D: Appl. Phys.* **44** 253001

Bílek P, Tungli J, Hoder T, Simek M and Bonaventura Z 2021 Electron–neutral bremsstrahlung radiation fingerprints the initial stage of nanosecond discharge in liquid water *Plasma Sources Sci. Technol.* **30** 04LT01

Bogen P, Conrads H, Gatti G and Kohlhaas W J 1968 Continuum radiation source of high intensity *Soc. Am.* **58** 203

Bonaventura Z, Tungli J, Bílek P and Šimek M 2021 Electron multiplication and avalanching in nanovoids at the initial stage of nanosecond discharge in liquid water *Plasma Sources Sci. Technol.* **30** 065023

Bray I, Konovalov D A and McCarthy I E 1991 Coupled-channel optical calculation of electron-hydrogen scattering: elastic scattering from 0.5 to 30 eV *Phys. Rev.* A **43** 5874

Bruggeman P J *et al* 2016 Plasma–liquid interactions: a review and roadmap *Plasma Sources Sci. Technol.* **25** 053002

Bruggeman P J and Leys C 2009 Non-thermal plasmas in and in contact with liquids *J. Phys. D: Appl. Phys.* **42** 053001

Bruggeman P J, Schram D, Gonzalez M A, Rego R, Kong M G and Leys C 2009 Characterization of a direct dc-excited discharge in water by optical emission spectroscopy *Plasma Source Sci. Technol.* **18** 025017

Bruggeman P J, Verreycken T, Gonzalez M A, Walsh J L, Kong M G, Leys C and Schram D 2010 Optical emission spectroscopy as a diagnostic for plasmas in liquids: opportunities and pitfalls *J. Phys. D: Appl. Phys.* **43** 124005–13

Bulanov S S *et al* 2010 Generation of GeV protons from 1 PW laser interaction with near critical density targets *Phys. Plasmas* **17** 043105

Burm K T A L 2004 Continuum radiation in a high pressure argon–mercury lamp *Plasma Sources Sci. Technol.* **13** 387–94

Buzulutskov A, Shemyakina E, Bondar A, Dolgov A, Frolov E, Nosov V, Oleynikov V, Shekhtman L and Sokolov A 2018 Revealing neutral bremsstrahlung in two-phase argon electroluminescence *Astropart. Phys.* **103** 29–40

Ceccato P H, Guaitella O, Le Gloahec M R and Rousseau A 2010 Time-resolved nanosecond imaging of the propagation of a corona-like plasma discharge in water at positive applied voltage polarity *J. Phys. D: Appl. Phys.* **43** 175202

Chauveau S, Deron C, Perrin M Y, Riviere P and Soufiani A 2003 Radiative transfer in LTE air plasmas for temperatures up to 15,000 K *J. Quantum Spectrosc. Radiat. Transfer* **77** 113

de Regt J M, van Dijk J, van der Mullen J J A M and Schram D C 1995 Components of continuum radiation in an inductively coupled plasma *J. Phys. D: Appl. Phys.* **28** 40

Dobrynin D, Seepersad Y, Pekker M, Shneider M, Fridman G and Fridman A A 2013 Non-equilibrium nanosecond-pulsed plasma generation in the liquid phase (water, PDMS) without bubbles: fast imaging, spectroscopy and leader-type model *J. Phys. D: Appl. Phys.* **46** 105201

Fantz U, Schalk B and Behringer K 2000 Calculation and interpretation of the continuum radiation of hydrogen molecules *New J. Phys.* **2** 7.1–7.15

Fichet P, Mauchien P, Wagner J-F and Moulin C 2001 Quantitative elemental determination in water and oil by laser induced breakdown spectroscopy *Anal. Chim. Acta* **429** 269–78

Foster J E 2017 Plasma-based water purification: challenges and prospects for the future *Phys. Plasmas* **24** 055501

Francois J P 1974 On the calculation of the self-absorption in spherical radioactive sources *Nucl. Instrum. Methods* **117** 153–6

Frommhold L 1998 Electron-atom bremsstrahlung and the sonoluminescence of rare gas bubbles *Phys. Rev.* E **58** 1899

Geltman S 1965 Continuum states of H^{-} and the free-free absorption coefficient *Astrophys. J.* **141** 376

Geltman S 1973 Free-free radiation in electron-neutral atom collisions *J. Quant. Spectrosc. Radiat. Transfer* **13** 601–13

Gigosos M A, Gonzalez M A and Cardenoso V 2003 Computer simulated Balmer-alpha, -beta and -gamma Stark line profiles for non-equilibrium plasmas diagnostics *Spectrochim. Acta* B **58** 1489–504

Griem H R 1964 *Plasma Spectroscopy* (McGraw-Hill)

Grosse K, Held J, Kai M and von Keudell A 2019 Nanosecond plasmas in water: ignition, cavitation and plasma parameters *Plasma Sources Sci. Technol.* **28** 085003

Grosse K, Schulz-von der Gathen V and von Keudell A 2020 Nanosecond pulsed discharges in distilled water: I. Continuum radiation and plasma ignition *Plasma Sources Sci. Technol.* **29** 095008

Hagelaar G J M and Pitchford L C 2005 Solving the Boltzmann equation to obtain electron transport coefficients and rate coefficients for fluid models *Plasma Sources Sci. Technol.* **14** 722–33

Hammer D and Frommhold L 2002 Light emission of sonoluminescent bubbles containing a rare gas and water vapor *Phys. Rev.* E **65** 046309

Hayashi M 1987 *Electron Collision Cross Sections for Molecules Determined from Beam and Swarm Data Swarm Studies and Inelastic Electron–Molecule Collisions* ed L C Pitchford *et al* (Springer) pp 167–87

Hoffer P, Prukner V, Schmidt J and Simek M 2020 Picosecond interferometry and analysis of pressure fields around nanosecond microdischarge filaments that develop in deionized water Japan *J. Appl. Phys.* **59** SHHA08

Hoffer P, Prukner V, Schmidt J and Šimek M 2021 Shockwaves evolving on nanosecond timescales around individual micro-discharge filaments in deionised water *J. Appl. Phys.* **54** 285202

Hueso J L, Rico V J, Cotrino J, Mateos J M J and Elipe A R G 2009 Water plasmas for the revalorisation of heavy oils and cokes from petroleum refining *Environ. Sci. Technol.* **43** 2557–62

Huiskamp T, Beckers F J C M, van Heesch E J M and Pemen A J M 2016 B-dot and D-dot sensors for (sub) nanosecond high-voltage and high-current pulse measurements *IEEE Sens. J.* **16** 3792–801

Hutchinson I H 2002 *Principles of Plasma Diagnostics* 2nd edn (Cambridge University Press)

Itikawa Y 1974 Momentum-transfer cross sections for electron collisions with atoms and molecules *At. Data Nucl. Data Tables* **14** 1–10

Itikawa Y and Ichimura A 1990 Cross sections for collisions of electrons and photons with atomic oxygen *J. Phys. Chem. Ref. Data* **19** 637

Itikawa Y and Mason N 2005 Cross sections for electron collisions with water molecules *J. Phys. Chem. Ref. Data* **34** 1–22

Khalid S, Kappus B, Weninger K and Putterman S 2012 Opacity and transport measurements reveal that dilute plasma models of sonoluminescence are not valid *Phys. Rev. Lett.* **108** 104302

Kielkopf J and Allard N 2014 Shift and width of the Balmer series Hα line at high electron density in a laser-produced plasma *J. Phys. B: At. Mol. Opt. Phys.* **47** 155701

Kierzkowska-Pawlak H, Tyczkowski J, Jarota A and Abramczyk H 2019 Hydrogen production in liquid water by femtosecond laser-induced plasma *Appl. Energy* **247** 24

Kolb J F, Joshi R P, Xiao S and Schoenbach K H 2008 Streamers in water and other dielectric liquids *J. Phys. D: Appl. Phys.* **41** 234007

Konjevic N, Ivkovic M and Sakan N 2012 Hydrogen Balmer lines for low electron number density plasma diagnostics *Spectrochim. Acta* B **76** 16–26

Krettek O, Pottkämper P, Cignoni P, Tschulik K and von Keudell A 2024 Creation of tungsten and platinum nanoparticles from nanosecond plasmas in water *J. Appl. Phys.* **57** 485201

Laher R R and Gilmore F R 1990 Updated excitation and ionization cross sections for electron impact on atomic oxygen *J. Phys. Chem. Ref. Data* **19** 277

Laux C O 1993 Optical diagnostics and radiative emission of air plasma *PhD Thesis* Stanford University

Laux C O, Spence T G, Kruger C H and Zare R N 2003 Optical diagnostics of atmospheric pressure air plasmas *Plasma Sources Sci. Technol.* **12** 125–38

Lavrov B P, Melnikov A S, Kaning M and Roepcke J 1999 UV continuum emission and diagnostics of hydrogen containing nonequilibrium plasmas *Phys. Rev.* E **59** 3526–43

Levko D, Sharma A and Raja L L 2017 Non-thermal plasma ethanol reforming in bubbles immersed in liquids *J. Phys. D: Appl. Phys.* **50** 085202

Lewis T J 2003 Breakdown initiating mechanisms at electrode interfaces in liquids *IEEE Trans. Dielectr. Electr. Insul.* **10** 948–55

Li Y, Li L, Wen J, Zhang J, Wang L and Zhang G 2020 Towards an improved understanding of nanosecond-pulse discharge initiation in water: from cavitation to electron multiplication *Plasma Sources Sci. Technol.* **29** 075005

Locke B R, Sato M, Sunka P, Hofman M R and Chang J S 2006 Electrohydrolic discharge and nonthermal plasma for water treatment *Ind. Eng. Chem. Res.* **45** 882–905

Luo Y 2019 Experimental and numerical study of nanosecond pulsed water containing discharges *PhD Thesis* University of Minnesota

Luo Y, Lietz A M, Yatom S, Kushner M J and Bruggeman P J 2019 Plasma kinetics in a nanosecond pulsed filamentary discharge sustained in Ar–H_2O and H_2O *J. Phys. D: Appl. Phys.* **52** 044003

Marinov I, Starikovskaia S and Rousseau A 2014 Dynamics of plasma evolution in a nanosecond underwater discharge *J. Phys. D: Appl. Phys.* **47** 224017

Mededovic S and Locke B R 2007 Primary chemical reactions in pulsed electrical discharge channels in water *J. Phys. D: Appl. Phys.* **40** 7734–46

Mjolsness R C and Ruppel H M 1967 Contribution of inverse neutral bremsstrahlung to the absorption coefficient of heated air *J. Quant. Spectrosc. Radiat. Transfer* **7** 423–7

Mukherjee M, Basu M and Ghosh A S 1987 Elastic electron-hydrogen scattering at intermediate energies *Phys. Rev.* A **36** 937

Nayak G, Simeni M S, Rosato J, Sadeghi N and Bruggeman P J 2021 Characterization of an RF-driven argon plasma at atmospheric pressure using broadband absorption and optical emission spectroscopy *J. Appl. Phys.* **128** 243302

Nikiforov A Y, Leys C, Gonzalez M A and Walsh J L 2015 Electron density measurement in atmospheric pressure plasma jets: stark broadening of hydrogenated and nonhydrogenated lines *Plasma Sources Sci. Technol.* **24** 034001

Park S, Choe W, Youn Moon S and Park J 2014 Electron density and temperature measurement by continuum radiation emitted from weakly ionized atmospheric pressure plasmas *Appl. Phys. Lett.* **104** 084103

Pekker M and Shneider M N 2015 Pre-breakdown cavitation nanopores in the dielectric fluid in the inhomogeneous, pulsed electric fields *J. Phys. D: Appl. Phys.* **48** 424009

Penner S S 1959 *Quantitative Molecular Spectroscopy and Gas Emissivities* vol 12 (Addison-Wesley)

Pitchford L C *et al* 2017 LXCat: an open-access, web-based platform for data needed for modeling low temperature plasmas *Plasma Process Polym.* **14** 1600098

Pongrác B, Šimek M, Člupek M, Babický V and Lukeš P 2018 Spectroscopic characteristics of Hα/OI atomic lines generated by nanosecond pulsed corona-like discharge in deionized water *J. Phys. D: Appl. Phys.* **51** 124001

Sainct F P, Urabe K, Pannier E, Lacoste D A and Laux C O 2020 Electron number density measurements in nanosecond repetitively pulsed discharges in water vapor at atmospheric pressure *Plasma Sources Sci. Technol.* **29** 025017

Sato M, Ohgiyama T and Clements J S 1996 Formation of chemical species and their effects on microorganisms using a pulsed high-voltage discharge in water *IEEE Trans. Ind. Appl.* **32** 106–12

Seepersad Y, Pekker M, Shneider M N, Dobrynin D and Fridman A 2013a On the electrostrictive mechanism of nanosecond-pulsed breakdown in liquid phase *J. Phys. D: Appl. Phys.* **46** 162001

Seepersad Y, Pekker M, Shneider M N, Fridman A and Dobrynin D 2013b Investigation of positive and negative modes of nanosecond pulsed discharge in water and electrostriction model of initiation *J. Phys. D: Appl. Phys.* **46** 355201

Sharkov E A 2003 *Passive Microwave Remote Sensing of the Earth: Physical Foundations* (Springer)

Shneider M N and Pekker M 2013 Dielectric fluid in inhomogeneous pulsed electric field *Phys. Rev.* E **87** 043004

Šimek M, Hoffer P, Tungli J, Prukner V, Schmidt J, Bílek P and Bonaventura Z 2020a Investigation of the initial phases of nanosecond discharges in liquid water *Plasma Sources Sci. Technol.* **29** 064001

Šimek M, Hoffer P , Prukner V and Schmidt J 2020b Disentangling dark and luminous phases of nanosecond discharges developing in liquid water *Plasma Sources Sci. Technol.* **29** 095001

Šimek M, Pongrác B, Babický V, Člupek M and Lukeš P 2017 Luminous phase of nanosecond discharge in deionized water: morphology, propagation velocity and optical emission *Plasma Sources Sci. Technol.* **26** 07LT01

Starikovskiy A, Yang Y, Cho Y I and Fridman A 2011 Non-equilibrium plasma in liquid water: dynamics of generation and quenching *Plasma Source Sci. Technol.* **20** 024003

Taghizadeh L, Nikiforov A Y, Morent R, van der Mullen J J A M and Leys C 2014 Determination of the electron temperature of atmospheric pressure argon plasmas by absolute line intensities and a collisional radiative model *Plasma Proc. Polym.* **11** 777–86

Taylor R L and Caledonia G 1969 Experimental determination of the cross-sections for neutral Bremsstrahlung: I. Ne, Ar and Xe *J. Quant. Spectrosc. Radiat. Transfer* **9** 657–79

Tomita K *et al* 2015 Development of a collective Thomson scattering system for laser-produced tin plasmas for extreme-ultraviolet light sources *Appl. Phys. Express* **8** 126101

Tomita K *et al* 2017 Time-resolved two-dimensional profiles of electron density and temperature of laser-produced tin plasmas for extreme-ultraviolet lithography light sources *Sci. Rep.* **7** 12328

van der Horst R M, Verreycken T, van Veldhuizen E M and Bruggeman P J 2012 Time-resolved optical emission spectroscopy of nanosecond pulsed discharges in atmospheric pressure N2 and N2 /H2O mixtures *J. Phys. D: Appl. Phys.* **45** 345201

Vegiri A 2004 Reorientational relaxation and rotational–translational coupling in water clusters in a dc external electric field *J. Mol. Liq.* **110** 155–68

Versolato O O 2019 Physics of laser-driven tin plasma sources of EUV radiation for nanolithography *Plasma Sources Sci. Technol.* **28** 08300

Von Keudell A, Grosse K and Schulz-von der Gathen V 2020 Nanosecond pulsed discharges in distilled water-Part II: line emission and plasma propagation *Plasma Sources Sci. Technol.* **29** 085021

Wang J, Simeni M S, Rong M and Bruggeman P J 2021 Absolute OH density and gas temperature measurements by laser induced fluorescence in a microsecond pulsed discharge generated in a conductive NaCl solution *Plasma Sources Sci. Technol.* **30** 075016

Webb M R and Hieftje G M 2009 Spectrochemical analysis by using discharge devices with solution electrodes *Anal. Chem.* **81** 862–7

Wen J, Li Y, Li L, Ni Z, Li Y and Zhang G 2020 Experimental observations and interpretations of bubble-induced discharges under microsecond pulsed voltages in water *J. Phys. D: Appl. Phys.* **53** 425208

Wilbers A T M, Kroesen G M W, Timmermans C J and Schram D C 1991 The continuum emission of an arc plasma *J. Quant. Spectrosc. Radiat. Transfer* **45** 1–10

Xiong Q, Nikiforov A, González M A, Leys C and Lu X P 2013 Characterization of an atmospheric helium plasma jet by relative and absolute optical emission spectroscopy *Plasma Sources Sci. Technol.* **22** 015011–24

Zel'dovich Y B and Raizer Y P 1966 *Physics of Shock Waves and High-Temperature Phenomena* (Academic)